Application of quantitative X-ray photoelectron spectroscopy (XPS) imaging: investigation of Ni-Cr-Mo alloys exposed to crevice corrosion solution

Brad Kobe,[a]* Martin Badley,[a,b] Jeffrey D. Henderson,[b]
Samantha Anderson,[b] Mark C. Biesinger[a] and Dave Shoesmith[a,b]

This paper explores quantitative X-ray photoelectron spectroscopy imaging on three different Ni-Cr-Mo Hastelloy® alloys (BC-1, C-22 and G-30) with differing Cr and Mo contents. The alloys were subjected to a simulated critical crevice corrosion solution. Ni-based alloys have been shown to exhibit excellent resistance to a range of corrosive media due to the formation of an inert oxide layer, primarily containing Cr and Mo. However, these alloys may rapidly corrode in the crevice environment produced by seams, gaskets or deposits of debris on the alloy surface. Understanding how the oxide film is influenced by the Cr and Mo content is crucial in determining an optimal alloy composition that reduces or suppresses the possibility of crevice corrosion. The protective oxide films are very thin in nature, generally several nanometers. XPS imaging was used to monitor changes in oxide film composition and to correlate the distribution of Cr and Mo to the grain structure of the alloys. Copyright © 2017 John Wiley & Sons, Ltd.

Keywords: XPS; image processing; EBSD; corrosion; crevice corrosion

Introduction

Routine XPS imaging has been around for approximately two decades.[1] The initial approach involved collecting XPS images at a specific energy and then subtracting and dividing by the background. Although this method compensates for differences in the photoelectric background and sample topography, the resulting images often have poor signal to noise, particularly with trace species and elements with smaller photoelectron cross-sections. This method also requires one to specify all the elements of interest during collection, without the option of any post analytical identification. The development of image-spectra data sets as a function of binding energy allows for greater flexibility during instrument setup and post processing of the data.[2] Improvements in the design of electron analyzers and delay-line detectors have facilitated fast collection times of these large image-spectra data sets and allow for true quantitative analyses.[3–6] The application of multivariate analysis on these large XPS data sets provides a method for the extraction of spectral and image information not apparently obvious.[7] Over the years, principal component analysis (PCA) methods have become more efficient at removing artifacts and noise from XPS image data sets by sorting and reducing the number of factors to compute using singular value decomposition and nonlinear iterative partial least squares routines.[8,9] XPS imaging has been successfully applied to a wide variety of applications from adhesion issues of polymethyl methacrylate,[10] 3D imaging of nanocomposites,[11] evaluation of wear scars[12] and the differentiation of similar carbon chemical states.[13]

In this paper, quantitative XPS imaging was used to investigate the role of Mo in the corrosion resistance of Ni-Cr-Mo alloys under the conditions expected during crevice corrosion, a form of localized corrosion. In general, Ni-based alloys have been shown to exhibit excellent resistance to a range of corrosive media due to formation of an inert oxide layer, primarily containing Cr and Mo. Cr forms a Cr_2O_3 barrier layer at the alloy/oxide interface, while Mo segregates to the outer regions of the film, i.e. the oxide/solution interface.[14,15] In the event of film breakdown, the deposition of Mo-rich corrosion products is believed to help repassivate the defect sites.[16] Despite the presence of this oxide film, these alloys may rapidly corrode in the crevice environment that could develop in occluded (crevice) locations. Such a situation could be produced by the presence of seams, gaskets or deposits of debris on the alloy surface. Within an active crevice, the solution composition is anticipated to change according to the critical crevice solution (CCS) theory outlined by Oldfield and Sutton.[17] This theory describes the development of an anaerobic HCl solution

* Correspondence to: Brad Kobe, Surface Science Western, The University of Western Ontario, 999 Collip Circle, Suite LL31, London, ON N6G 0J3, Canada.
  E-mail: bkobe@uwo.ca

a Surface Science Western, The University of Western Ontario, 999 Collip Circle, Suite LL31, London, ON, N6G 0J3, Canada

b Department of Chemistry, The University of Western Ontario, 1151 Richmond Street, London, ON, N6A 5B7, Canada

1345

within the creviced region. The development of such a solution may challenge the integrity of the oxide film due to the high solubility of Cr_2O_3 at low pH. As a result, understanding how the oxide film in this environment is influenced by the Mo content is crucial in determining an optimal alloy composition that reduces or suppresses the possibility of crevice corrosion. The protective oxide films are very thin, typically several nanometers. XPS imaging was used to monitor changes in oxide film composition and to correlate the distribution of Cr and Mo to the grain structure of the alloys.

Experimental

Sample preparation and treatment

Alloy samples were provided by Haynes International® (Kokomo, IN, USA) and the nominal compositions are given in Table 1. Alloy coupons were cut to 1 cm × 1 cm × 0.635 cm in size. They were then ground using wet silicon carbide and sonicated to remove any debris before being further polished to a final 1 μm diamond finish. Subsequently, some samples were etched to expose the underlying microstructure and enhance the quality of diffraction patterns obtained by electron backscattered diffraction. Different etching procedures were used for the various alloys because of differences in corrosion resistance. Hastelloy® G-30 was etched by manual swabbing with a mixture (3 : 2 : 2) of HCl, CH_3COOH and HNO_3. Hastelloy® C-22 and BC-1 were electrochemically etched in an oxalic acid solution (10 wt.%) by the application of 0.2 A cm^{-2} for 10–15 s.

Prior to subsequent analyses, three microhardness indents were made on each coupon serving as reference points to align the XPS images with the scanning electron microscopy images. The coupons were then immersed for a total of 20 h in a simulated CCS of 1 M HCl + 2 M NaCl at 75°C. During this 20-h period, coupons were intermittently removed for electron imaging after 2, 8, 14 and 20 h (total). An additional set of coupons, not exposed to acidic conditions following polishing, was stored under vacuum for a 24-h period prior to analyses and are referred to as initial 'as-polished' samples.

Instrumentation

The XPS analyses of the three corroded alloys were carried out using a Kratos AXIS Nova spectrometer (Kratos Analytical Ltd, Manchester, UK) equipped with a spherical mirror analyzer combined with a delay-line detector. A monochromatic Al Kα source (15 mA and 14 kV) was used along with a charge neutralizer system. The instrument work function was calibrated to give a binding energy of 83.96 eV for the Au 4f$_{7/2}$ line of metallic gold, and the spectrometer dispersion was adjusted to give a binding energy of 932.62 eV for the Cu 2p$_{3/2}$ line of metallic copper. Binding energy accuracy is ±0.025 eV. All image data sets were collected

using a field of view of approximately 725 micron × 725 microns and medium resolution imaging mode. The elemental survey image scans were collected from 1100 eV – 0 eV at a step size of 1 eV and a pass energy of 160 eV. Each image was collected for 16 s for a total collection time of approximately 5 h. The high resolution image datasets were collected for Cr and Mo using a step size of 0.1 eV and a pass energy of 40 eV. Chemical state images were collected for 300 s for a total time of approximately 5 h per element.

Image analysis methodology

All spectra and image data sets were analyzed using CasaXPS software (Version 2.3.18dev1.1j).[18] An outlier filter was first applied to the image data sets with a 70% threshold value with five iterations. The outlier filter was applied before PCA analysis to help discriminate between potentially weak XPS signals and noise by reducing local anomalous pixel intensities.[9] The data were then sorted using an Optimum Scaling (OpS) routine to determine the number of significant factors. This approach separated the important information from the noise while using a smaller number of images for efficient computation. Once the number of abstract factors was determined, PCA analysis (OpS) was applied to the entire image data set (Predictive OpS). The resulting images were then converted to spectra. The elements were identified, and a Shirley background correction was applied. All the processed spectra were then converted back to images and quantified.

EBSD characterization

Prior to corrosion in the CCS, the alloy coupons were analyzed by electron backscatter diffraction (EBSD) to provide information on the grain orientation and the relative energies of the grain boundaries. The EBSD was conducted on the Hitachi SU6600 field emission scanning electron microscope located in the ZAPLab (Department of Earth Sciences, UWO). The field emission scanning electron microscope was outfitted with a HKL Nordly EBSD detector to collect Kikuchi patterns. Data analysis was carried out using the HKL Channel 5 software suite (Oxford Instruments). All crystal orientation information was indexed according to the fcc crystal structure.

Results

Survey data collected from the three alloys in the as-polished condition prior to any corrosion are presented in Table 2. All three alloys show a significant amount of carbon contamination. However, the relative amounts of Ni, Cr and Mo follow the general trend expected for each alloy. G-30 shows the highest Cr content

Table 1. Alloy composition (wt.%) as reported by Haynes International®

Alloys	Ni	Cr	Mo	W	Fe	Cu	Nb	Al	V	Co	Mn	Si	C
BC-1	62	15	22	—	2	—	—	0.5	—	1	0.25	0.08	0.01
C-22	56	22	13	3	3	0.5	—	—	0.35	2.5	0.5	0.08	0.01
G-30	43	30	5.5	2.5	15	2	0.8	—	—	5	1.5	0.8	0.03

Table 2. Summary of elemental concentration (atomic %) of the image area for each alloy

Alloy	C	O	Ni	Cr	Mo	W	Nb	Cu	Cl
BC-1 (as-polished)	42.6	24.7	16.2	4.8	6.4	—	—	—	—
BC-1 (after Corrosion)	51.8	29.6	5.9	4.8	7	—	—	—	0.9
C-22 (as-polished)	47.4	23.5	14	9.2	5.9	—	—	—	—
C-22 (after Corrosion)	48.6	31.4	6	4.5	7.1	—	—	—	2.4
G-30 (as-polished)	52.4	26.6	7	13	1.2	—	—	—	—
G-30 (after Corrosion)	43.2	38.5	4.1	9.1	3.4	0.9	0.5	0.3	—

and lowest Mo content compared with alloys C-22 and BC-1. Approximately 25% oxygen is also present on the surface of the alloys.

The grain orientations and grain boundary energies of the three Ni-Cr-Mo alloys were measured using EBSD before corrosion in the CCS. The EBSD images, presented in Fig. 1, show that the grain size for G-30 is significantly larger than for C-22 and BC-1 that have similar grain sizes. The green and red lines overlaid on the grain structure represent $\sum 3$ boundaries and random ($\sum > 29$) boundaries, respectively. The Σ notation denotes the reciprocal of coincident points between adjacent grains. $\Sigma 3$ boundaries would have one third of their lattice points coincident if the grains were overlapped and are considered low energy boundaries. By contrast, random grain boundaries that exhibit very little overlap are considered high energy. As a result, the $\sum 3$ boundaries are expected to be more corrosion resistant than the random grain boundaries.[19,20] All three alloys contain a large number of $\sum 3$ sites, approximately 70% compared with the random high energy sites, Fig. 1. The $\sum 3$ sites are mostly associated with twinning locations, while the grain boundaries are random sites. Of particular interest are the triple points where three random grain boundaries meet: A number of these sites are visible for all three alloys. It has been reported that localized breakdown of the oxide film can occur at these locations.[21] The goal of this study is to correlate the initial microstructure to the oxide film structure after CCS exposure.

After exposure to the CCS for a total of 20 h, BSE images (Fig. 2) were taken of the same region. The grain structure is clearly visible on all three alloys. Alloy G-30 shows preferential etching of the random grain boundaries and localized pitting on the grain surfaces, while alloys C-22 and BC-1 did not show the same general surface pitting and grain boundary attack. For these alloys, minor damage was observed only on random grain boundaries.

Using the reference microhardness indents, the same area on each alloy coupon examined by EBSD was then analyzed using XPS imaging to correlate the distribution of Cr and Mo with potential breakdown sites. For each data set, the spectra at each pixel were added together and quantified to provide an average concentration on the surface. A summary of the elements (atomic %) detected for each imaged area after corrosion is presented in Table 2. A high amount of carbon contamination remains on the surface of all three alloys after corrosion. All three alloys show a small increase in oxygen concentration after corrosion, suggesting an increase in oxide film thickness relative to the initial 'as-polished' coupons. The Ni and Cr levels decreased after corrosion for all three alloys compared with the initial as-polished surface. In contrast, the Mo content increased after corrosion. Ni and Cr are both highly soluble in CCS, while Mo has a solubility that decreases as the pH decreases.[22]

The XPS images, Fig. 3, show the distribution of Ni, Cr, Mo and O on the surface of each alloy following 20-h exposure to CCS. The thermal scale, to the right of each image, corresponds to the minimum (black areas) and maximum (white) concentration for that element (atomic %). For alloy G-30, the images for O and Cr are clearly correlated, along with Ni to a lesser extent. The Ni, Cr and Mo show some correlation for C-22, and BC-1 shows Ni and O are closely correlated. However, understanding the distributions of Cr and Mo is of particular interest because they represent the major components of the oxide and is considered responsible for protecting the alloys from corrosion. Thus, for G-30, the Cr and Mo are anticorrelated, but for C-22 and BC-1, there is overlap between Cr and Mo.
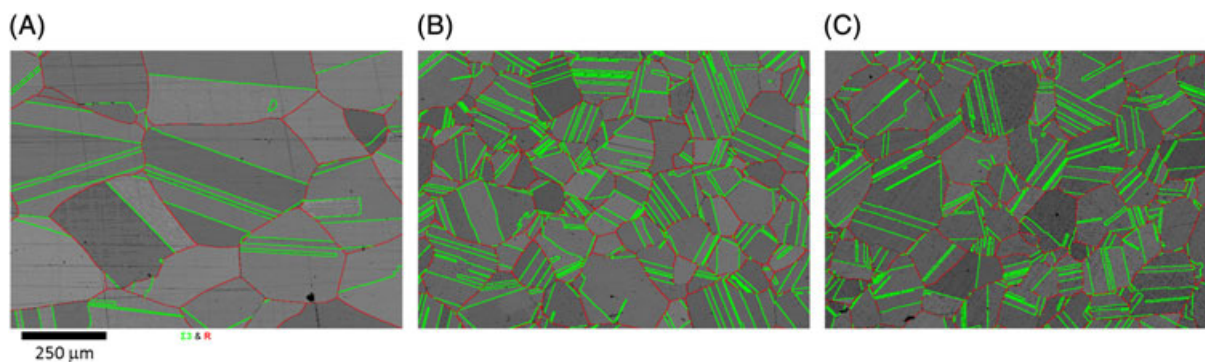

Figure 1. Electron backscatter diffraction band contrast images for alloys before corrosion in critical crevice solution (a) G-30, (b) C-22 and (c) BC-1. The $\Sigma 3$ boundaries are green, while the random boundaries are red.
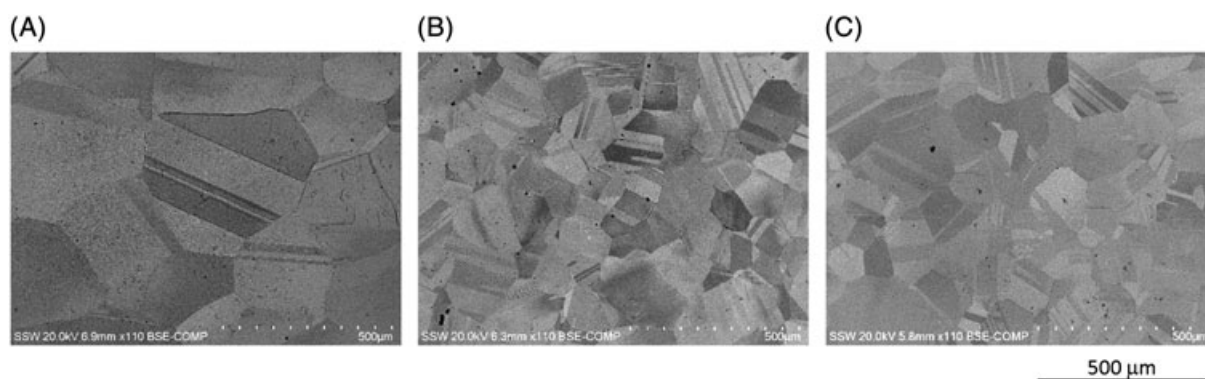

Figure 2. SEM images of the three alloys after critical crevice solution immersion (a) G-30, (b) C-22 and (c) BC-1.
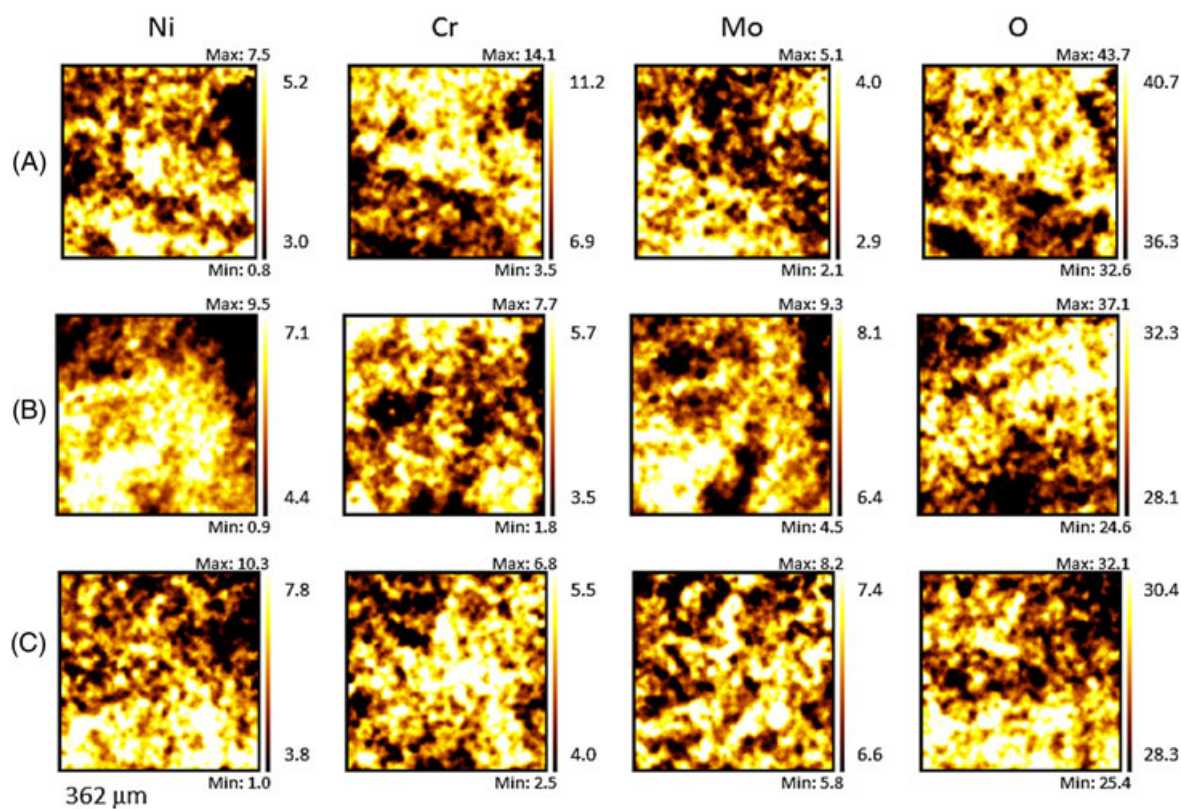
Figure 3. Elemental XPS survey images showing Ni, Cr, Mo and O for each alloy after critical crevice solution (a) G-30, (b) C-22 and (c) BC-1.

To visualize the data, the images for Cr (green) and Mo (red) were overlaid, Fig. 4. The yellow areas indicate that both Cr and Mo are present at the same location. The overlaid image for G-30 shows large distinct areas of Cr and Mo with very little overlap. The red areas suggest that corrosion is occurring over large areas of the sample surface with Mo being relocated to areas experiencing corrosion.[16] The overlaid image for alloy C-22 shows distinct Cr and Mo sites, but the overall coverage is less extensive than observed for G-30. There are also some areas where Cr and Mo overlap (yellow areas). The increased number of smaller Mo sites suggests that corrosion is localized and does not spread across the surface. For BC-1, the surface shows significant overlap of Cr and Mo (yellow areas), with only very small Mo sites, suggesting a more even distribution of the two elements as expected on a passive surface. Zhang *et al.* found that the thin passive film on Ni-Cr-Mo alloys consists of a layered structure with an inner Cr_2O_3 layer and an outer surface with MoO_3.[15]

To determine whether there is a correlation between the grain boundary structure and the accumulation of Mo due to corrosion, the Mo-Cr XPS images from Fig. 4 were overlaid on the EBSD images from Fig. 1, the resulting overlaid images are presented in Figure 5. No clear correlation between the locations of the Mo (corrosion sites) and the $\sum 3$ and random grain boundaries was observed on G30®. This result is not unexpected because corrosion damage is extensive both on the grains and grain boundaries.

Corrosion on alloy C-22 was much less extensive compared with that on alloy G-30. The damage was more localized with some overlap of Mo and Cr. Although difficult to align properly with the finer grain structure of C-22, the distribution of Mo suggests that corrosion damage is more localized to the random grain boundaries. Thin Mo regions appear to run along grain boundaries and in some cases, encircle grains. This morphology supports the claim that preferential passive film breakdown occurs at the random grain
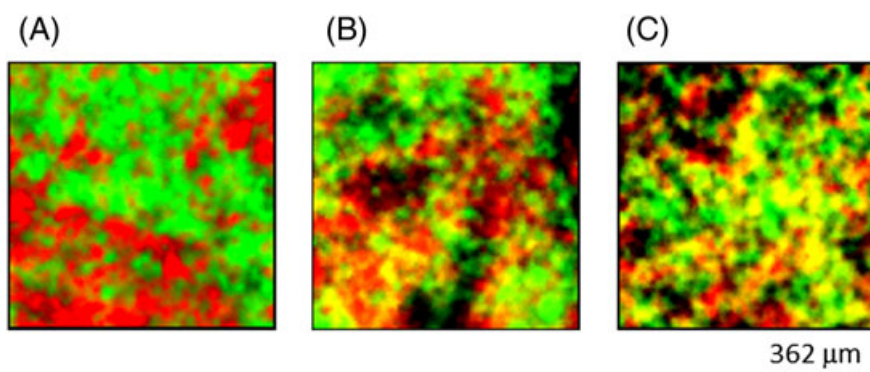

Figure 4. Overlaid XPS survey images of molybdenum (red), chromium (green) and mixture (yellow) for alloys (a) G-30, (b) C-22 and (c) BC-1.
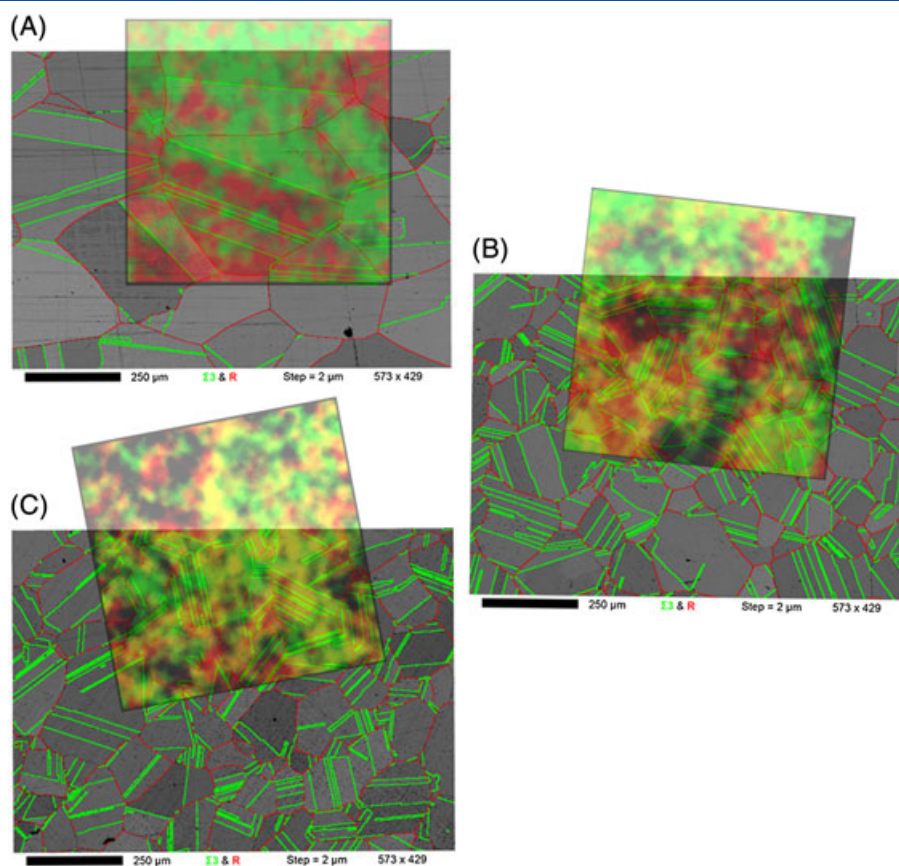
Figure 5. Overlaid XPS survey images of molybdenum (red), chromium (green) and mixed (yellow) with the electron backscatter diffraction images for (a) G-30, (b) C-22, (c) BC-1 showing Σ3 and random grain boundaries.

boundaries, typically observed between individual grains. There are also some areas were individual grains appear to be Mo-rich.

The least amount of damage was observed on BC-1, where Mo and Cr coexist more evenly across the surface of the alloy. This co-existence suggests a stable passive film is maintained on the alloy surface during exposure to CCS. There does not appear to be any correlation between Mo enrichment and the location of either Σ3 or random grain boundaries. These results demonstrate the influence of a high Mo content in maintaining passivity possibly by preventing significant local film breakdown events.

High resolution chemical state images were collected to show the distribution of Mo oxidation states on the surface of alloy G-30. G-30 was chosen because it shows the greatest correlation with

the large grain structure. The Mo 3D high resolution spectrum from the imaged area is presented in Fig. 6a. The spectrum was fit using three sets of Mo $3d_{5/2}$-$3d_{3/2}$ spin-orbit doublets with a peak separation of 3.13 eV and 3 : 2 area ratios. The metallic peaks were fit with an asymmetric peak-shape based on a standard sputter cleaned Mo metal sample. The results show that three species are present Mo – metal, Mo(IV) and Mo(VI). Approximately half of the Mo is attributed to Mo(VI), the oxidized form anticipated at passive film breakdown sites.[18] Smaller amounts of Mo(IV) and some metal Mo are also present. The overlaid XPS image, Fig. 6b, shows distinct regions for Mo (metal), Mo(IV) and Mo(VI). To help show if there is any correlation between the three Mo states and potentially active grain boundaries, the XPS images of Mo, Mo(IV) and Mo(VI) are
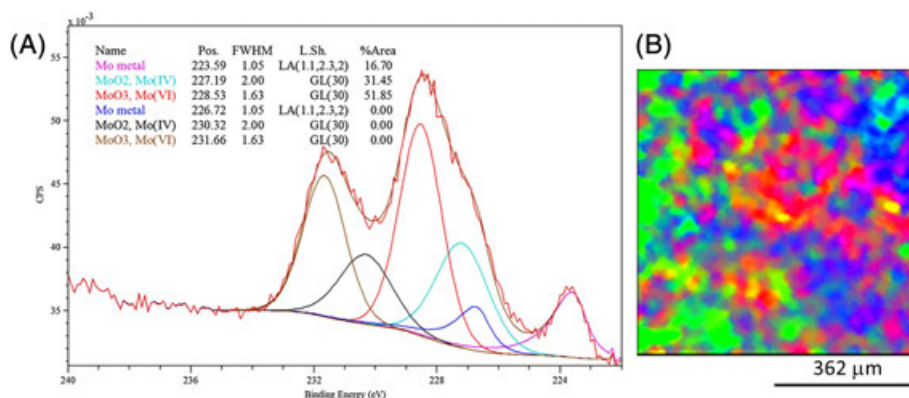

Figure 6. (a) High resolution Mo 3D spectrum and (b) overlaid XPS images for Mo metal (red), Mo(IV) (blue) and Mo(VI) (green) for G-30.
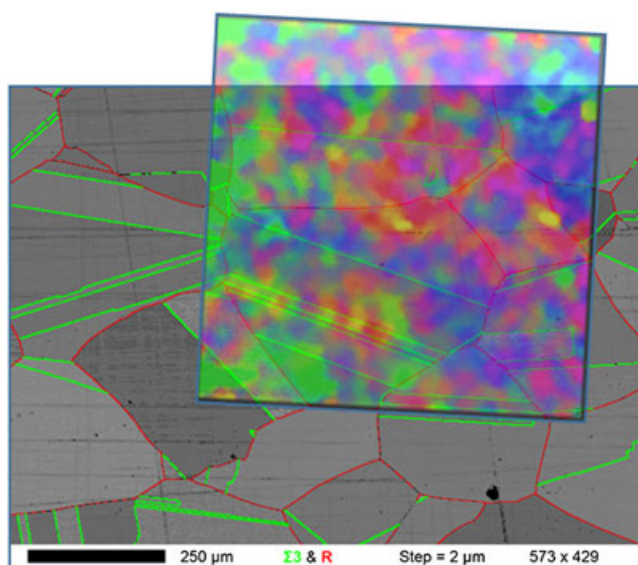
Figure 7. Overlaid XPS images of Mo metal (red), Mo IV (blue) and Mo VI (green) for sample G-30 superimposed with the electron backscatter diffraction image showing the Σ3 and random grain boundaries.

overlaid with the EBSD image (Fig. 7). In general, Mo(VI) covered large areas of the surface and did not appear to be selectively associated with specific grain boundaries. This is likely a consequence of the widespread corrosion damage on this alloy that Fig. 2 shows was not confined to local sites.

Conclusion

XPS imaging was carried out on three corrosion resistant alloys, G-30, C-22 and BC-1. Quantitative elemental and chemical state information from the XPS images were correlated with SEM imaging and EBSD data to ascertain the role of Mo in the corrosion resistance of the three Ni-Cr-Mo alloys.

The EBSD data showed that all three alloys contained a large number of Σ3 grain boundaries, approximately 70% compared with the random high energy boundaries. XPS imaging made it possible to compare the random grain boundaries with the distribution of Mo. Alloy G-30 showed Mo present over large areas with little correlation to grain boundaries. Corrosion on alloy C-22 was much less extensive compared with that on alloy G-30. The distribution of Mo suggests that corrosion damage was more localized to the random grain boundaries. The least amount of damage was observed on BC-1, where Mo and Cr coexist more evenly across the surface of the alloy. This coexistence suggests a stable passive film was maintained during exposure to the CCS. There does not appear to be any correlation between Mo enrichment and the location of either Σ3 or random grain boundaries.

High resolution chemical state XPS imaging conducted on G-30 showed the distribution of three species Mo – metal, Mo(IV) and Mo(VI). Approximately half of the Mo was attributed to Mo(VI), the oxidized form anticipated at passive film breakdown sites. However, Mo(VI) covered large areas of the surface and did not appear to be selectively associated with specific grain boundaries. This was likely a consequence of the widespread corrosion damage on this alloy. However, further investigation is needed under less aggressive conditions on images collected at higher magnification to detect differences on the smaller grains for C-22 and BC-1.

References

[1] P. Y. Timbrell, M. K. Purchert, R. N. Lamb, *Surf. Interface Anal.*, **1994**, *21*, 731–736.
[2] K. Artyushkova, J. E. Fulghum, *J. Electron. Spectrosc. Relat. Phenom.*, **2001**, *121*, 33–35.
[3] P. Coxon, J. Krixak, M. Humpherson, I. R. M. Wardell, *J. Electron. Spectrosc. Relat. Phenom.*, **1990**, *52*, 821–836.
[4] Kratos Analytical Limited, European Patent Office 0 458 498 A2, **1991** (S.C. Page).
[5] U. Vohrer, C. Blomfield, S. C. Page, A. J. Roberts, *Appl. Surf. Sci.*, **2005**, *61*, 61–65.
[6] A. J. Roberts, S. C. Page, K. Takahashi, *J. Surf Anal.*, **2007**, *14*, 160.
[7] K. Artyushkova, J. E. Fulghum, *Surf. Interface Anal.*, **2002**, *33*, 185–195.
[8] J. Walton, *Surf. Interface Anal.*, **2007**, *39*, 337–342.
[9] S. Bechu, M. Richard-Plouet, V. Fernadez, J. Walton, N. Fairley, *Surf. Interface Anal.*, **2016**, *48*, 301–309.
[10] H. Piao, N. Fairley, J. Walton, *Surf. Interface Anal.*, **2013**, *45*, 1742–1750.
[11] K. Artyushkova, *J. Electron. Spectrosc. Relat. Phenom.*, **2010**, *178-179*, 292–302.
[12] C. Gabler, N. Dörr, G. Allmaier, *Tribol. Int.*, **2014**, *80*, 90–97.
[13] A. J. Barlow, S. Popescu, K. Artyushkova, O. Scott, N. Sano, J. Hedley, P. J. Cumpson, *Carbon*, **2016**, *107*, 190–197.
[14] X. Zhang, D. W. Shoesmith, *Corros. Sci.*, **2013**, *76*, 424–431.
[15] X. Zhang, D. Zagidulin, D. W. Shoesmith, *Electrochim. Acta*, **2013**, *89*, 814–822.
[16] N. Ebrahimi, P. Jakupi, J. J. Noël, D. W. Shoesmith, *Corrosion*, **2015**, *71*, 1441–1451.
[17] J. W. Oldfield, W. H. Sutton, *Br. Corros J.*, **1978**, *13*, 13–22.
[18] N. Fairley, 2016 http://www.casaxps.com, © Casa Software Ltd. **2016**. [Last accessed in 2016].
[19] P. Jakupi, J. J. Noël, D. W. Shoesmith, *Electrochem. Solid St.*, **2010**, *13*, C1–C3.
[20] S. Ranganathan, *Acta Crystallogr.*, **1966**, *21*, 197–199.
[21] N. Ebrahimi, P. Jakupi, A. Korinek, I. Barker, D. E. Moser, D. W. Shoesmith, *J. Electochem. Soc.*, **2016**, *163*, C232–C239.
[22] C. F. Baes, R. E. Mesmer, *The Hydrolysis of Cations*, Krieger Pub Co, Florida, **1986**, p. 256.